Bistatic Rough Surface Scattering at P-Band in Grand Mesa Based on Lidar Observations of Surface Roughness and Topography

Haokui Xu, *Student Member, IEEE*, Leung Tsang, *Life Fellow, IEEE*, Xiaolan Xu, *Senior Member, IEEE*, Simon Yueh, *Fellow, IEEE*, Steven A. Margulis, and Rashmi Shah, *Senior Member, IEEE*

***Abstract*—In this article, we use the analytical Kirchhoff solution (AKS) and numerical Kirchhoff approach to study the bistatic scattering field (γ) from mountain terrain at P-band frequency. The study area is Grand Mesa, Colorado, USA, and the properties of land surface roughness are extracted from airborne lidar surveys. The bistatic scattering coefficient γ of variance fields, denoted byγ_v, for several cases of radar resolutions over a 3.6 km by 3.6 km area are calculated at various scattering azimuth angles. Based on the lidar measurements, the land surface is decomposed into $f_2 + f_3$, where f_3 is 30 m of deterministic planar patches to approximate the coarse topography and f_2 is modeled by random rough surfaces with correlation functions. Surface roughness statistics derived from the Lidar data give a typical root mean square height of 0.07 m and a correlation length of 3.6 m for f_2. The mean values of slopes of f_3 are 1.3° and 0° with a standard deviation of 1° each, respectively in the x and y directions. Simulations using AKS show that the values of bistatic scattering coefficients for the variance of scattered fields can reach above 10 dB over a range of azimuth angles ϕ_s in the vicinity of the specular direction. Even in mountainous regions, the value of the γ_v around the forward scattering direction is much larger than that for radar backscattering, and thus could support the use of a synthetic aperture radar concept based on signals of opportunity with data acquisition near the forward direction.**

***Index Terms*—Analytical Kirchhoff solution, lidar data, P-band, rough surface, signal of opportunities.**

I. Introduction

MICROWAVE remote sensing at P-band (216–415 MHz) can be used to retrieve root zone moisture [1], biomass [2], [3], snow water equivalent [4], and polar subsurface temperature [5]. The BIOMASS mission of the European Space Agency provides a resolution of 200 m using a P-band synthetic aperture radar (SAR) with the potential of measuring biomass and root zone moisture.

However, the use of space-borne P-band radar for remote sensing over North America and most of Europe is restricted due to the fact that the P-band remote sensing radar will inevitably interfere with the performance of US Space Objects Tracking Radar, which has been designated as the primary user of 435 MHz band.

In recent years, the concept of Signals of Opportunity (SoOp) has gained popularity because of the lower costs associated with using transmitters on existing navigation and communication satellites. Satellites with receivers have been launched to measure the reflected signals from the earth's surface. At L-band, the Global Navigation Satellite System Reflectometry (GNSS-R) has been extensively used since the launch of Techdemosat-1(TDS-1) by the U.K. in 2014 [6].

Other GNSS-R missions include the Cyclone Global Navigation Satellite System (CYGNSS) [7] launched by NASA in 2016, Bufeng [8] launched by China in 2019, and Hydro-GNSS-R to be launched by Italy [9]. GNSS-R data have been applied to the retrieval of ocean wind speed [10], sea ice thickness [11], and monitoring wetland changes [12], and soil moisture [13], [14], [15]. Machine learning methods have also been applied to retrieve geophysical parameters [16]. However, the resolution of the GNSS-R systems is typically 20 to 30 km due to the limits of bandwidth in both signal and Doppler shift. In addition, the L-band signals are strongly attenuated by the vegetation and forest coverage.

An SAR concept based on SoOp in P-band has been proposed [17] that utilizes the signal from the Mobile User Objective System (MUOS) [18]. MUOS has four operating satellites at geosynchronous altitudes, broadcasting at two frequencies (360–380 MHz and 240–270 MHz) within P-band. With a constellation of low earth orbit-based receivers, a high resolution of 100 m can be achieved [17]. To achieve an adequate signal to noise ratio (SNR) for the P-band SoOp SAR, the strength of bistatic scattering coefficients of land surfaces is crucial. This needs to be studied for retrieval of snow water equivalent in mountainous terrain where seasonal snow resides. Different from classical GNSS-R systems, the SAR concept would also need the knowledge of bistatic scattering off the specular direction, usually, in azimuthal scattering direction.

Manuscript received 10 July 2023; revised 29 August 2023; accepted 27 September 2023. Date of publication 12 October 2023; date of current version 23 November 2023. This work was supported by the NASA Remote Sensing Theory Program. *(Corresponding author: Leung Tsang.)*

Haokui Xu and Leung Tsang are with the Radiation Laboratory, Department of Electrical and Computer Engineering, University of Michigan, Ann Arbor, MI 48105 USA (e-mail: xuhaoku@umich.edu; leutsang@umich.edu).

Xiaolan Xu, Simon Yueh, and Rashmi Shah are with the Jet Propulsion Laboratory, California Institute of Technology, Pasadena, CA 91109 USA (e-mail: xiaolan.xu@jpl.nasa.gov; simon.h.yueh@jpl.nasa.gov; rashmi.shah@jpl.nasa.gov).

Steven A. Margulis is with the Department of Civil and Environmental Engineering, University of California, Los Angeles, CA 90095 USA (e-mail: margulis@seas.ucla.edu).

Digital Object Identifier 10.1109/JSTARS.2023.3324217

In our previous reflectometry studies of land surfaces at L- band [19], we decompose land surfaces into three spatial scales. The smallest scale (f_1) is random and has a scale with a typical root mean square (rms) height of under 4 cm and a correlation length several times the rms height. The largest scale (f_3) is around 30 m. The f_3 is deterministic and is planar with well-defined slopes in both *x* and *y* directions. An intermediate scale (f_2) is used to bridge the gap. In this article, we use Lidar measurements [20] with a typical spatial resolution of meters to provide a characterization of f_2. For the present case of P-band with a wavelength (81 cm) much larger than $f_1 (h_1 < 4\,\text{cm})$ we ignore f_1 in this article.

The rough surface and topography effects on GNSS-R data at L-band have been studied by the GO method [21], [22], [23], the Improved GO method [24], and the SAVERS model [25]. We have also developed two methods 1) NKA (numerical Kirchhoff approach) [26], and 2) AKS (analytic Kirchhoff solution) [19]. Intercomparison study has also been made on these methods in [27].

There are major differences in rough surface scattering between radar (monostatic) backscattering and the forward (bistatic) scattering used in reflectometry. The former has a large difference in horizontal *k* vector between the incident direction and the return direction which is opposite to the incident direction [19], [21] The contributions of monostatic radar come primarily from diffuse scattering due to rough surface features smaller than or comparable to the wavelength. In the case of reflectometry, the bistatic scattering direction is in the vicinity of the specular direction. At a 40° incidence angle, the radar cross section of a rough surface in the vicinity of the specular direction is expected to be much larger (∼20 dB) than for backscattering in the L-band, which is typically in the range of –10 to –20 dB). As shown in previous L band studies [27], the radar cross sections in reflectometry are strongly influenced by topography in addition to random roughness.

In this article, to investigate the characteristics of surface scattering at P band near the vicinity of specular direction (ϕ_s from 0° to 10°), in the context of mountainous terrain as represented in Grand Mesa, Colorado, NKA [26] and AKS [19] are applied. We use Lidar data collected during NASA SnowEx 2020 project [20] to derive f_2 and f_3. The properties of f_2 and f_3 are used for the input of Kirchhoff models.

The rest of this article is organized as follows. We summarize the AKS model and NKA methods in Section II. In Section III, we describe the method to extract f_2 and f_3. In Section IV, we illustrate the basic results of 30 m patches with various statistical properties of f_2 and various tiling slopes of f_3. The AKS and NKA results are shown to be in good agreement. In Section V, we illustrate the simulated bistatic scattering coefficients over Grand Mesa over a range of azimuthal angles. The bistatic scattering is found to be of significance. Finally, Section VI concludes the article.

II. Surface Scattering Models

Details of the AKS and NKA are documented in [19] and [26], respectively. The major characteristics of AKS are summarized here. We first describe the representation of land surface in this model.

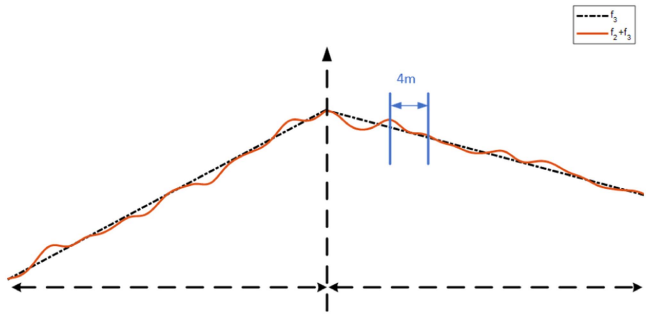

Fig. 1. Land surface represented with multiple scales. Black dash line: Coarse topography f_3, projection on *x*–*y* plane (e.g., 30 m). Yellow line: $f_2 + f_3$, where the "4 m" in the figure is an example of the correlation length of f_2. In this article, the small scale f_1 is ignored due to its smallness compared to wave length at P band (81 cm).

As shown in Fig. 1, for the P band, the land surface is decomposed into two scales: $f(x, y) = f_2\,(x, y) + f_3(x, y)$. The topography is approximated by deterministic planar patches f_3. Each of the f_3 planar patches has definite slopes in the horizontal (x, y) directions. By approximation, it means that the size of the planar patch in f_3 must be small enough to correctly approximate the topography. For the results in this article, a size of 30 m x 30 m for a single f_3 patch is adequate. Thus, we have a total of 14 400 30 m by 30 m f_3 patches within the study area of 3.6 km by 3.6 km. The scales f_2 are modeled as random profiles, superimposed on f_3.

Since the study is designed to provide results in support of an SAR concept with a spatial resolution of about 100 m [17], the bistatic scattering coefficients for several 30 m patches are of interest. In this article, we use resolutions of 60, 120, and 240 m to assess the impact of spatial resolution limited by SAR processing as examples.

In AKS and NKA, we have both coherent field contributions and incoherent field contributions. The coherent and the incoherent are the mean and variances of the field, respectively. In the main text, we will discuss the incoherent field.

The bistatic scattering coefficient of the scattered field for right-hand circularly polarized incidence and left-hand circularly polarized scattering for the incoherent component of a single 30 m x 30 m f_{3n} is given by

$$\gamma_v^n = \frac{\cos\theta_i}{\pi}\left|\frac{R_v(\theta_i) - R_h(\theta_i)}{2}\right|^2$$

$$2\pi k^2 \int_0^\infty d_\rho \rho J_0\left(\rho\sqrt{(k_{dxn} + k_{dzn}p_{n3})^2 + (k_{dyn} + k_{dzn}q_{n3})^2}\right.$$

$$\{\exp[-k_{dzn}^2 h_{2n}^2(1 - C_{2n}(\rho))] - \exp(-k_{dzn}^2 h_{2n}^2)\} \quad (1)$$

where *n* denotes the index of the 30 m f_3 in the total 14 400 f_3 patches within the area, $R_v(\theta_i)$ and $R_h(\theta_i)$ are the Fresnel reflection coefficients, respectively, for vertical and horizontal polarization with an incident angle at θ_i and k is the wave number for the frequency of 370 MHz. The integral accounts for the effects of f_2 and f_3. Inside the Bessel function (J_0), the incident direction is defined by θ_i and the scattering direction is defined

by θ_{sn} and ϕ_{sn}, the wave vector for the incident and scattering waves are given as follows:

$$\overrightarrow{k_i} = k\sin\theta_i\hat{x} - k\cos\theta_i\hat{z}$$

$$\overrightarrow{k_s} = k\sin\theta_{sn}\cos\phi_{sn}\hat{x} + k\sin\theta_{sn}\sin\phi_{sn}\hat{y} + k\cos\theta_{sn}\hat{z}.$$

The difference is thus given as $\vec{k}_{dn} = \vec{k}_{in} - \vec{k}_{sn}$. The parameters p_{n3} and q_{n3} are the slopes of this particular $f_3(x, y)$ patch, accounting for the tilting of f_3 patches. They are defined as the derivatives of $f_3(x, y)$ in x and y directions. h_{2n} and $C_{2n}(\rho)$ are the rms height and correlation function obtained from Lidar data on this particular f_3 patch.$C_{2n}(\rho)$ is constructed with Lidar data Details on obtaining these parameters from Lidar data are discussed in Section III.

After the bistatic scattering coefficients are computed for each 30 m patch, γ_{v}^{Np} for each resolution is obtained by the following equation:

$$\gamma_v^{N_p} = \frac{1}{N_p}\sum_{n=1}^{N_p}\gamma_v^n \tag{2}$$

where $\gamma_{\mathrm{v}}^{N_p}$ represents the bistatic scattering coefficient for N_p 30 m x 30 m patches within the resolution. For 60, 120, and 240 m resolution in this article, N_p corresponds to 4, 16, and 64, respectively. Each resolution will include the contribution from several 30 m $\times$ 30 m f_3 patches.

The bistatic scattering coefficient is defined as scattering cross section per unit area, and thus the incoherent γ is independent of the observation area.

In AKS we take the ensemble average over f_2, which is considered as a random profile. The averaging is taken "Analytically" for which "A" stands. The average is taken with an rms height and a correlation function [23], [24], [25], [26], [28], [29].

To validate the AKS solution, NKA is used. As from paper [26], the equation for NKA is as follows:

$$\overrightarrow{E}_s = \frac{ik\exp(ik(R_t+R_r))}{4\pi R_t R_r}\sqrt{\frac{\eta P_t G_t}{2\pi}}p_s \cdot \int dA' \exp(i\overrightarrow{k_d}\cdot\overrightarrow{r}')\overrightarrow{F}(\alpha,\beta) \tag{3}$$

where $\exp(i\overrightarrow{k_d}\cdot\overrightarrow{r'}) = \exp(i[k_{dx}+k_{dz}p_3]x' + [k_{dy}+k_{dz}q_3]y' + k_{dz}f_2(x',y'))$

In performing NKA, serval points need to be mentioned.

1) NKA performs the averaging of f_2 by the Monte Carlo method. Realizations of f_2 are generated based on the correlation function and scattered wave from each realization needs to be computed by (3). Thus, results from NKA show speckle effects. In this article, several hundred realizations of f_2 are used.
2) Averaging is taken over the realizations of the scattered field results. This is unlike AKS where the averaging is taken analytically using the correlation function of the profile.
3) On averaging over realizations, the speckle noise is decreased.
4) In numerical averaging, we obtain the coherent field which is the averaged field over the realizations. The incoherent field for each realization is obtained by subtraction of the mean field from the field. The variance of the field is then obtained using the incoherent field intensities for each realization.
5) In NKA, the integral in (3) needs to be performed numerically over the profile. The discretization of the profile needs to be much smaller than a wavelength. In this article, we use 5 cm. Since the Lidar profile data *f(x, y)* data is of 3 m resolution, we use a 2-D cubic spline to interpolate the lidar profile of *f(x, y)* into 5 cm. In generating the realizations, the random profiles are also at 5 cm spatial discretization.

In both AKS and NKA, averaging is not taken for f_3 since f_3 representing the topography is deterministic. The bistatic scattering coefficients for multiple patches were previously given in our paper [19] for the GNSS-R application.

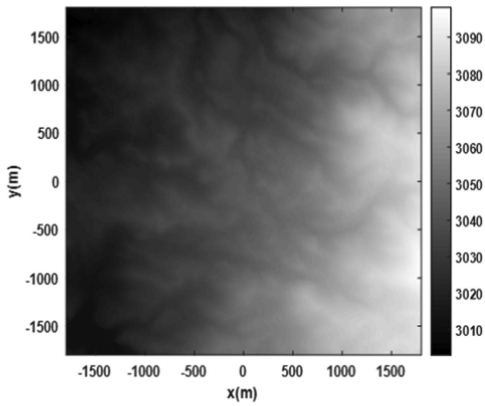

Fig. 2. Lidar elevation data (in meters) for the selected 3.6 km x 3.6 km area in Grand Mesa (39.05 N 108.13 W).

III. Extraction of Correlation Functions of f_2 and Slopes of f_3 in *x* and *y* Directions From Lidar Data

The properties of f_2 and f_3 presented here are derived from the ASO L4 Lidar Point Cloud 3-meter Digital Terrain model products. The lidar data were collected over Grand Mesa, Colorado, USA, during snow-free conditions as part of the NASA/JPL ASO aircraft survey campaigns [20]. The data set provides a 3 m horizontal resolution elevation map with a 1.7 cm vertical resolution.

We select an area of size 3.6 km x 3.6 km in dimension as shown in Fig. 2, which is analyzed for the surface roughness properties examined herein.

The planar patches of f_3 are first extracted. Fig. 3 shows the fitting of planar patches to the topography. Data in blue are the lidar data with 3 m resolution while the orange lines are the fitting to the profile using different patch sizes. Fig. 3 shows that the 30 m f_3 represents the topography very well compared to the other three larger patch sizes. Larger patch sizes such as 60 m, 120 m, and 240 m introduce significant errors in representing

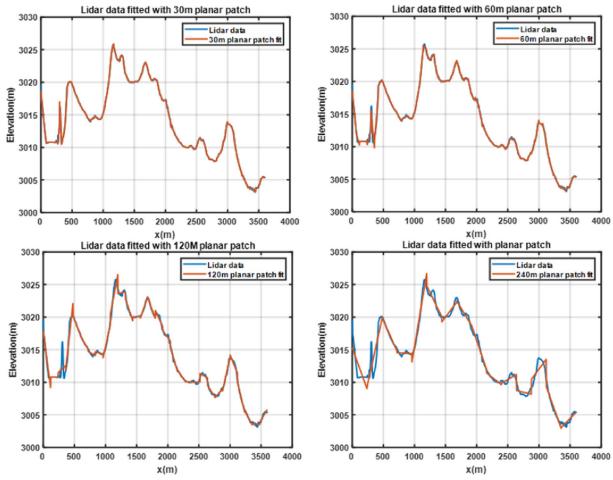

Fig. 3. Representing the land surface with different patch sizes. 30 m patch size is representing the land profile well. Other three larger patch sizes are creating errors.

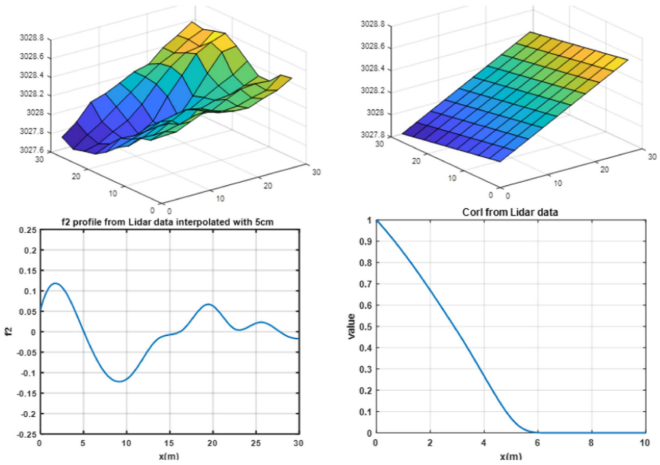

Fig. 4. Extraction of surface properties from lidar data. (a) 30 m x 30 m patch size in the *x*–*y* plane, and (b) f_3 (*x*,*y*) for the 30 m x 30 m patch. The planar surface is obtained by fitting the lidar data to a patch as in (a). (c) Example of the 1-D (x) profile from data. (d) Correlation function of the 1-D profile fitted.

the topography. Thus in this paper, we use 30m as the size of each f_3 planar patch size.

The Lidar data is treated as a profile of $f_2(x, y) + f_3(x, y)$. To obtain the land surface properties, we conducted the following steps: First, we divided the land surface with a 30 m x 30 m patch size in the *x*—*y* plane. Fig. 4(a) shows an example of a patch of f_3 from lidar data with a size of 30 m x 30 m in the *x*—*y* plane. The patch of Lidar data is then fitted to a plane of the same size on the *x*—*y* plane, as shown in Fig. 4(b). The planar patch in Fig. 4(b) is the $f_3(x, y)$ for this particular 30 m x 30 m data, where the patch defines a single value of the slopes in the *x* and *y* directions. The planar patch f_3 could be anisotropic with different slopes in *x* and *y*.

After subtracting out $f_3(x, y)$, what remains is the profile $f_2(x, y)$. To evaluate the rms height and correlation length, we interpolate the profile into a 5 cm horizontal resolution. 2-D

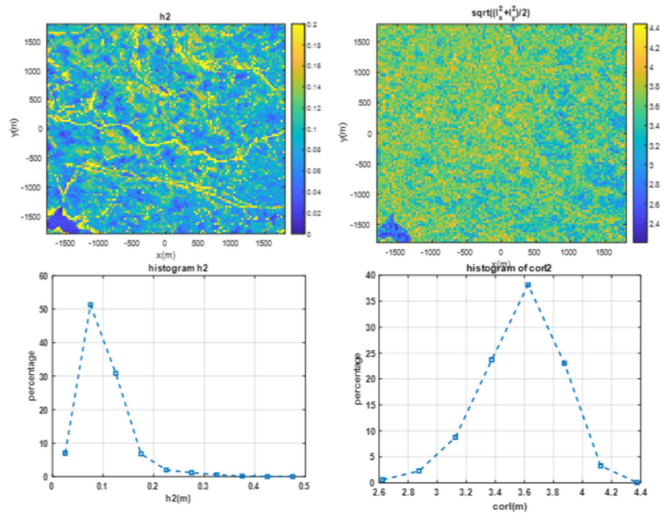

Fig. 5. Properties of f_2 (x,y) using a 30 m patch size. The upper two panels show the rms height and correlation length for each 30 m x 30 m patch in the 3.6 km x 3.6 km area.

interpolation over the $f_2(x, y)$. Thus, over a 30 m by 30 m patch, there are 600 by 600 = 360 000 points in f_2(*x*,*y*). Using these 360 000 points, we calculate the correlation function of this patch as follows. There are 600 1-D profiles in *x* and 600 1-D profiles in *y*.

An example of the 1-D profile is shown in Fig. 4(c). We directly calculate the rms height of the $f_2(x, y)$ surface for this patch as h_{2n}. For the correlation function, a 1-D profile in the *x* direction is taken as $f^i_{2x}(x)$, *i* is from 1 to 600. The correlation function is then calculated directly from this 1-D profile as $C^i_{2x}(x)$. The correlation function is normalized with respect to the peak value. The correlation function in the *x* direction is thus obtained by $C_{2x}\ (x) = <C^i_{2x}(x)>$ over *i*. The process is repeated for each of the 600 1-D profiles in *y* direction to obtain $C_{2y}(y)$. The correlation function of this particular f_3 is then obtained by $C_2\ (\rho) = \sqrt{\frac{1}{2}(C^2_{2x}(x) + C^2_{2y}(y))}$. The correlation length is thus obtained by $C_2(\rho)$ when the value is e^{-1}. Rms height and correlation length of f_2 is provided in Fig. 5 as maps and histograms. We find that f_2 is quite isotropic with only small difference between *x* and *y*. As shown in Fig. 6, the ratio of correlation lengths in the x and y directions are centered in the range of 0.9 to 1.1. This is unlike f_3 which is anisotropic and has different slopes in x and y as represented by p3n and q3n.

To illustrate the distribution of h_{2n} and l_{2n} pairs, a density plot is generated as in Fig. 7. As can be observed, the typical values of h_2 and l_2 are 7 cm and 3.55 m, respectively. Notice that the input to AKS is the correlation function $C_2(\rho)$ rather than the correlation length l. In this article, we use the extracted correlation function for each patch. For the area 3.6 km by 3.6 km by 3.6 km, there are 120 by 120 = 14 400 planar patches. We have extracted 14 400 correlation functions using the lidar data. We use these 14 400 calculated correlation functions, one for each patch, over the 3.6 km by 3.6 km area. This approach

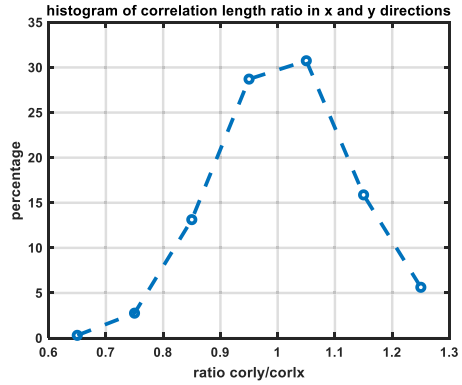

Fig. 6. Histogram of correlation length ratio for x and y directions. It is shown that most of the ratios lie in the range of 0.9 to 1.1. Showing that the land surface is close to isotropic.

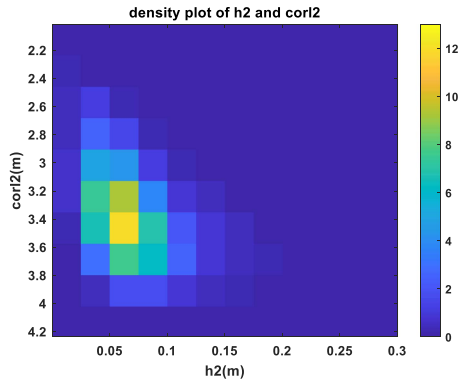

Fig. 7. Density plot of h2 and corl2 for f_2(x,y). The typical number would be $h = 7$ cm, corl = 3.55 m (color scale: Percentage).

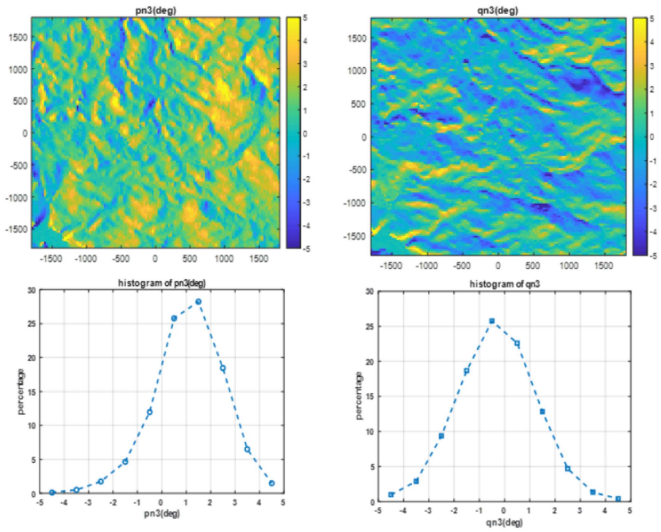

Fig. 8. Slopes of f_3 (x,y) patches with 30 m patch sizes.

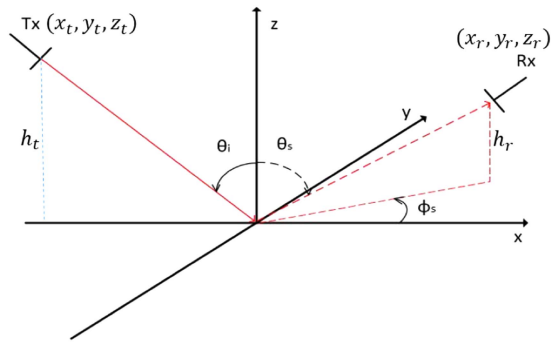

Fig. 9. Set up for the scattering geometry. Specular point is the origin. θ_i, θ_s are polar angles for incidence and scattering. ϕ_s is the scattering azimuthal angle. (x_t, y_t, z_t),(x_r, y_r, z_r) are the locations for transmitter and receiver.

thus accounts for the surface inhomogeneity in this particular 3.6 km x 3.6 km study area.

In Fig. 8, the distributions of slopes in the x and y directions for 30 m patches are shown. It can be observed that the slopes in the x (east-west) and y (north-south) directions are slightly different. The slope distribution in y is centered near zero, while there is a positive mean slope in x, consistent with the elevation map shown in Fig. 2, which shows a decreasing elevation from east to west.

For 30 m patches, p_{n3} has a mean value of 1.2° and a standard deviation of 1.33°. For q_{n3}, the mean value is 0° with a standard deviation of 1.5°. For each patch, the x and y slopes are usually quite different showing that topography is generally anisotropic. On the other hand, the f_2 correlation functions are more isotropic in the x and y directions. The results here will be used for the bistatic scattering study with AKS.

IV. Bistatic Results of Single Patches

In this section, we illustrate the results of single patches. The bistatic scattering coefficients are studied for the cases with and without f_3 and also for varying distances of patches from the center of the scene. The set up of the geometry is provided in Fig. 9 The bistatic scattering is illustrated as a function of azimuth angle ϕ_s. We use the typical number of $h_2 = 7$ cm and the correlation function that has the typical value of 3.57 m correlation length. AKS and NKA are both used. The permittivity is 5.5+2i. For NKA, a profile of f_2 is needed as input for each realization. We take the Fourier transform of the correlation function to obtain the power spectrum density and then generate profiles as input to NKA. The generation of the surface is discussed in Appendix A. 400 profiles of f_2 are used to generate the second moment of scattered waves. To reduce the effects of the coherent field, when calculating the variance of the fields, the patch size is enlarged to 60 m to reduce the angular spreading of the mean-field. For the f_2 only case, ϕ_s equals to 0° is not calculated for NKA due to the large peak from the mean field. The results in Figs. 10 and 11 are for the case when the patch is at the center with $(x,y) = (00)$ of the scene. Fig. 10 use the typical number of p_{n3} and q_{n3} slopes while in Fig. 11, an artificial slope p_{n3} of 3.4° is used to show the effect of large slope.

For the effects of f_3, we add the f_2 onto a tilted patch with $p_{n3} = 2^\circ$ and $q_{n3} = -1^\circ$, which are typical slopes in this area. The results of AKS and NKA results are shown in Fig. 10.

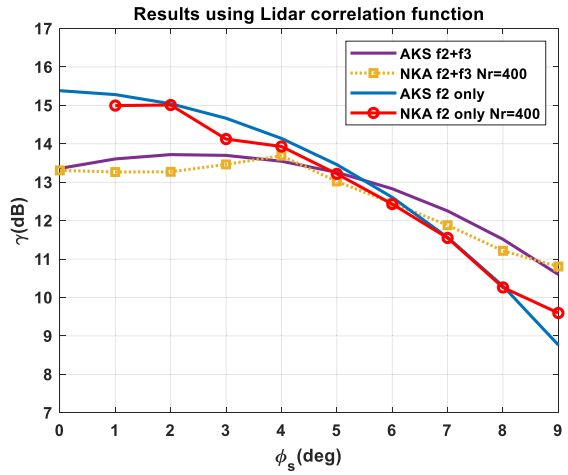

Fig. 10. AKS and NKA results for a single patch with and without f3. The planar patch f3 has a tilting effect.

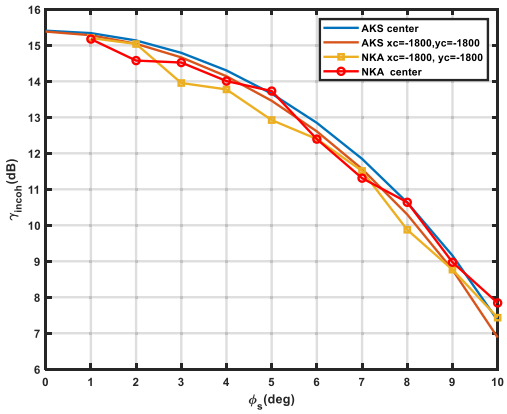

Fig. 12. Bistatic scattering coefficients for 30 m patch at and away from center(x-1800,y-1800). Due to the smallness of the area compared to the height of the transmitter and receiver, the incident and scattering direction does not have major changes. The difference is within 0.5 dB.

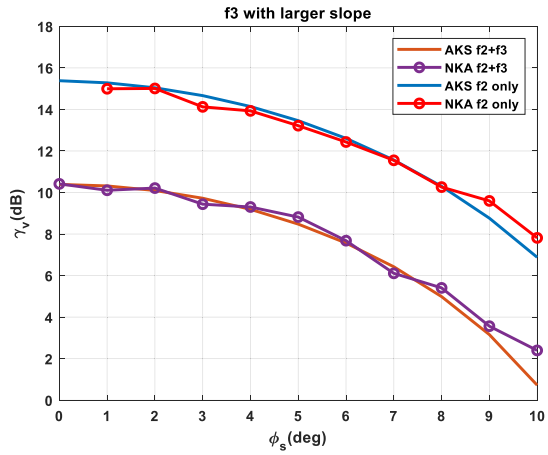

Fig. 11. Incoherent bistatic scattering coefficients with or without the effects of large f_3 slope. With an artificial slope of 3.5° in x direction, a reduction of 5 dB is observed. This is to show the effects of a large slope to the bistatic scattering coefficients.

The AKS and NKA results are in good agreement. Thus the AKS results are validated by NKA. The effects of slopes are also shown. The f_3 slopes reduce the peak value of the bistatic scattering coefficients. The f_3 slopes can also shift the peak value.

NKA and AKS results are also provided for a case where a large f_3 slope is used. The results are shown in Fig. 11, where a planar patch f3 with an artificial p_{n3} value of 0.06 (or 3.4°) is used, which has small fraction of patches in this area. The goal is to show the effects of large slope effects on the bistatic scattering coefficients. A large reduction of 5 dB is observed in the bistatic scattering coefficients in the near specular direction. This shows that the topographical slopes have strong effects on the bistatic scattering coefficients near the specular direction.

We next examine the bistatic scattering coefficients when the patch is placed at the corner of the observation area with coordinates (x,y) = (1.8 km,1.8 km). The results are shown in Fig. 12. There are no significant changes from the case where the patch is at the center of the scene. This is due to the high elevation of the transmitter and receiver compared to the size of the observation area.

In Appendix B, we illustrate and discuss the bistatic scattering coefficients of the coherent fields.

V. Bistatic Scattering Coefficients of Grand MESA

In this section, we discuss the bistatic scattering coefficients computed using AKS for the entire scene of 3.6 km by 3.6 km. We use the 14 400 calculated correlations functions, the h_2s and also the p_{n3} and q_{n3}s, one for each patch. The setup of simulations is shown in Fig. 9. For the soil permittivity, we use a value of 5.73+0.73i, which corresponds to a volumetric soil moisture of about 10%. A local scattering coordinate system is created with the origin at the center of the 3.6 km x 3.6 km area. The transmitter is set at the position of $(x_t, 0, z_t)$ on the geostationary orbit. The receiver is set at the position of (x_r, y_r, z_r) on the lower earth orbit. The coordinates on the x0-y plane for the transmitter and receiver are determined by the incidence angle (θ_i) and scattering angles (θ_s), respectively. The coordinates are provided as the following: $z_t = h_t$, $x_t = -\tan(\theta_i)h_t$, $z_r = h_r$, $x_r = \tan(\theta_i)\ \cos(\phi_s)hr$, $y_r = \tan(\theta_i)\sin(\phi_s)$, the annotations are provided in Fig. 9.

We first study the effects of the azimuth angles in the observation direction. In the simulation, we set $\theta_i = \theta_s = 40^\circ$ at the position of the center of the area of interest. The bistatic scattering coefficient of each 30 m f_3 is calculated with (1) using the h_{2n}, $C_{2n}(\rho)$, p_{n3}, and q_{n3} obtained from Section III. For azimuth angles, ϕ_s is set as 0°, 2.5°, 5°, 7°, and 10° to calculate γ_v and γ_m. We look at the resolutions of 60, 120, and 240 m. The results are obtained based on (2). That means each resolution needs to average over 4, 16, 64, 30 m x 30 m γ_vs within that particular resolution.

Results for γ_v from (2) for the 3.6 km x 3.6 km area with 60 m x 60 m resolution are illustrated in Fig. 13. As shown in Fig. 13(a) (specular direction), γ_v can be as large as 20 dB and is mostly above 10 dB. It can be observed that in the region around (1000 m, 500 m), a low γ_v region is shown. This is mainly due

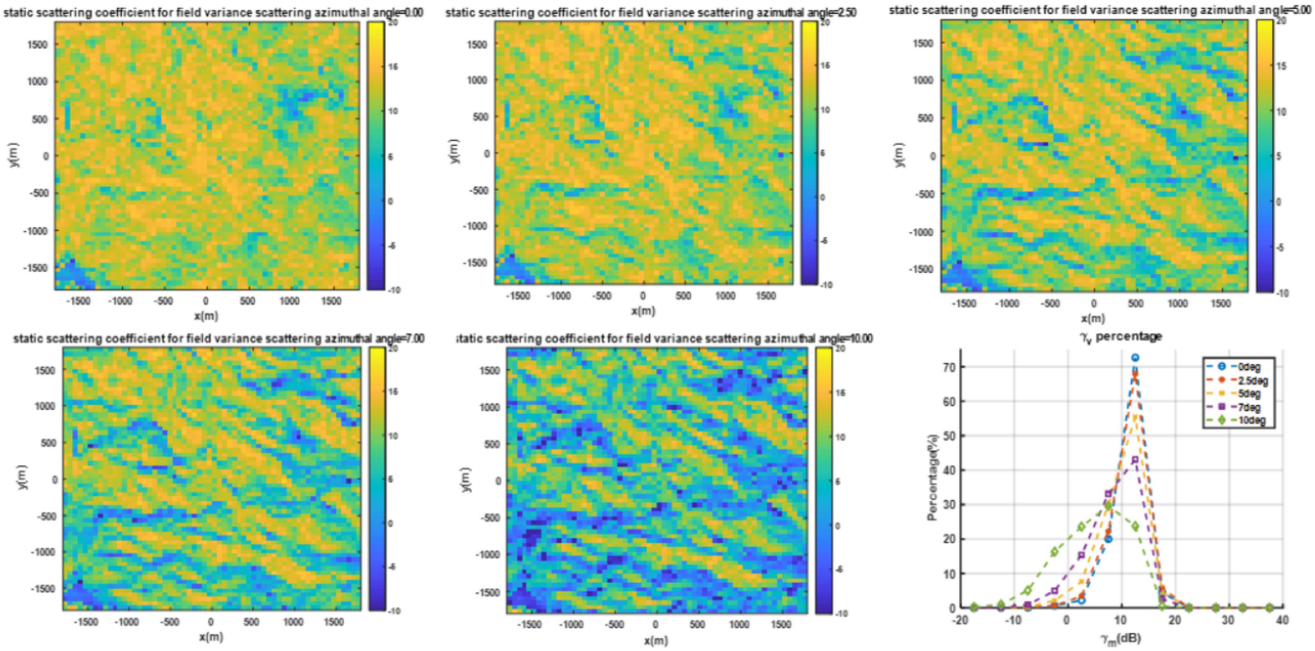

Fig. 13. γ_v (in dB) for 60 m x 60 m resolution over the 3.6 km x 3.6 km area using the results from Figs. 5 and 8. From panel (a) through (e), $\theta_i = \theta_s = 40°$, while ϕ_s are 0° to 2.5°, 5°, 7°, and 10°. γ_v decreases as the ϕ_s increases. The distribution of γ_v in dB is in panel f. It can be observed that the peak of γ_v decreases as ϕ_s increases.

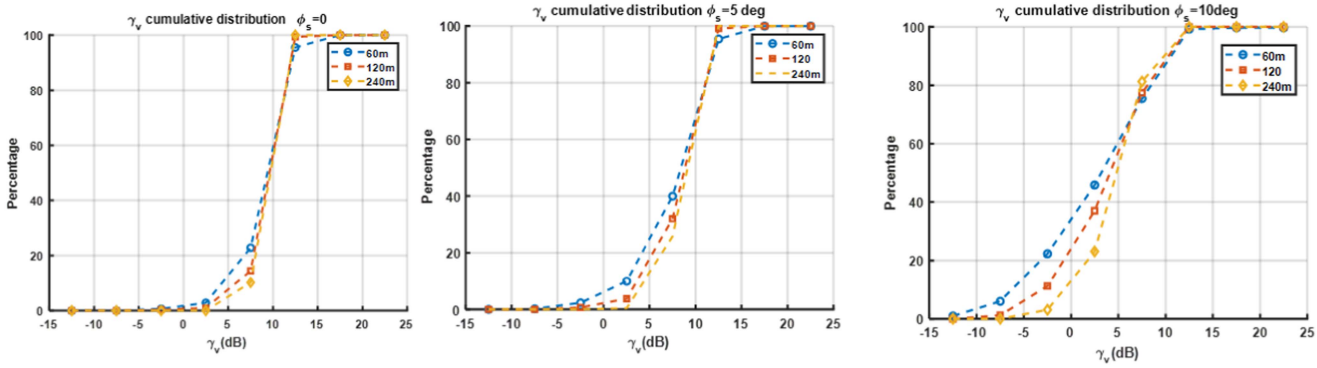

Fig. 14. Cumulative distribution of γ_v for different resolutions. The distributions are consistent.

to the large slopes for the corresponding region (see Fig. 7). The slopes of pn_3 in that region is larger than the other regions, reducing the scattered power in the receiver direction. This reduction is not due to the properties of f_2 since the rms height and correlation length do not show many differences compared to other regions. The spatial patterns of γ_v at the azimuth angles of 2°, 5°, 7°, and 10° are similar; however, γ_v decreases with the increase of ϕ_s as shown in Fig. 13(f). The peak of the histogram gradually moves to the lower value bins. But as shown in the case of $\phi_s = 10°$, about 10% of the patches within the region still have a value γ_v above 10 dB.

To further compare the effects of different resolutions, the cumulative distribution of the bistatic scattering coefficients is presented in Fig. 14. Azimuthal scattering angles of 0°, 5°, and 10° are provided with different resolutions. It is shown that the 3 resolutions are consistent with each other.

For a given radar system, the swath of measurement and the ability to detect the signal is determined by the gain pattern of the receiving antenna. High-gain antennas usually have small beam width, which makes the footprint on land (swath) small, while antenna with smaller gain will have a larger swath. For a given SNR, the large value of γ_v reduces the requirement of antenna gain, which allows a broader swath on land.

VI. Conclusion

In this article, we study the bistatic scattering coefficients for the mean and variance of the bistatic scattered field near the specular direction for P-band frequencies. Simulation parameters are obtained from the Lidar measurements over Grand Mesa. 30 m planar patches f_3 size is an appropriate choice for approximating land topography in Grand Mesa. Using the lidar

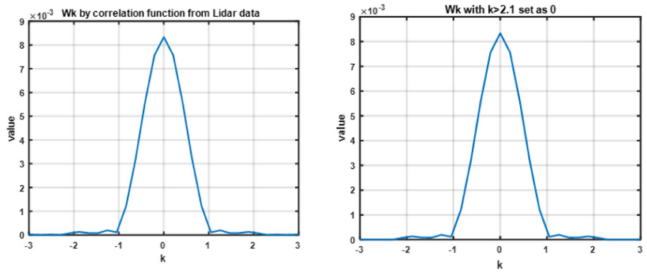

Fig. 15. Power spectrum density before and after truncating at 2.1, corresponding to 3 m of the lidar resolution.

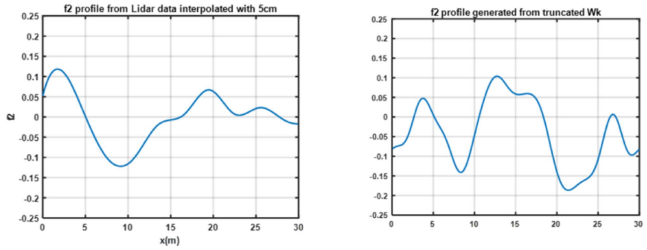

Fig. 16. Profile from lidar data and Wk generation.

data, we calculate the correlation function of f2 for each 30 m by 30 m patch for the 3.6 km by 3.6 km scene. AKS results are calculated for each 30 m by 30 m patch using the 14 400 calculated correlation functions.

Simulation results show that γ_v is of the highest significance: the value can be as large as 10 dB over a wide range of azimuth angles. The value decreases as ϕ_s increases but can be still significant with a value greater than 0 dB. Results show significant values of γ_v within 5° to 10° in azimuth from the specular direction, which will lead to a generally high SNR for SoOp reflectometry over a range of cross-track distances (swath), which is proportional to the feasible range of azimuth angle. The choice of f_3 can be adjusted based on the topography as f_3 are planar patches that approximate the topography. The size of f_3 can be larger when the topography has smaller slope than Grand Mesa. The size of f_3 can be smaller when the topography has larger slope than Grand Mesa. The same AKS model can still be applied for such cases.

APPENDIX

A. Generation of Profiles for NKA

We discuss the generation of random profiles f_2 based on the correlation functions. The correlation function obtained from Lidar data is symmetrical in the x and y directions. We thus perform a 2-D Fourier transform to obtain the power spectrum density of the surface. Since the resolution of Lidar data is 3 m, Wk components that are greater than 2.1 is ignored. With the Wk, we follow the method in [30] Chp.4 to generate the random profiles of $f_2(x, y)$. Examples of Wk and generated random profiles compared with Lidar data are shown in Figs. 15 and 16, respectively.

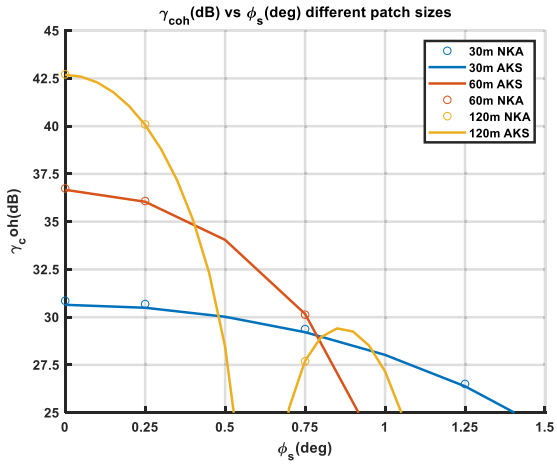

Fig. 17. Bistiatic scattering coefficient of mean field vs different $\phi_s(^\circ)$ patch sizes.

B. Results of Mean Field

The coherent field gamma is given in (B1).

For the mean field of each f_3 patch, the bi-static scattering coefficient is provided as follows:

$$\gamma_m^n = \frac{\cos\theta_i}{\pi}\left|\frac{R_v(\theta_i)-R_h(\theta_i)}{2}\right|^2\left|kL\exp\left(-\frac{k_{dzn}^2h_2^2}{2}\right)\right.$$
$$\left.\sin c\left[\left(\frac{k_{dnx}}{k_{dnz}}+p_{n3}\right)\frac{k_{dnz}L}{2}\right]\sin c\left[\left(\frac{k_{dny}}{k_{dnz}}+q_{n3}\right)\frac{k_{dnz}L}{2}\right]\right|^2 \quad \text{(B1)}$$

where the term $\exp(-\frac{1}{2}k_{dzn}^2h_2^2)$ account for the decay due to surface roughness. The sinc functions account for the beam width and the direction of the mean field.

In the comparison of (1) and (B1), it can be observed that γ_v is independent of area, however forγ_m, it is a function of the area. γ_m thus

1) increases with area;
2) becomes exponentially small with the increase of h_2;
3) is sharply peaked in the specular direction with decreasing angular width as observation area increases;
4) decreases sharply when there is a tilting due to f3 because the receiver is away from the specular direction of patch f_3.

Fig. 17 shows the scattering pattern of the mean field from AKS and NKA. Only f_2 is calculated with the profiles placed in the center of the observation area. Different patch sizes of 30, 60, and 120 m are used. The rms height and correlation function used is the same as in Section IV. As stated previously, the bistatic scattering coefficients of the mean-field are proportional to the area in the specular direction. The angular width of the mean field is also sharpened as the planar patch size increases.. The inclusions of bistatic scattering coefficients of coherent field need to be considered together with the instrument characteristics of the receivers of P band reflectometry.

REFERENCES

[1] A. Etminan, A. Tabatabaeenejad, and M. Moghaddam, "Retrieving root-zone soil moisture profile from P-band radar via hybrid global and local optimization," *IEEE Trans. Geosci. Remote Sens.*, vol. 58, no. 8, pp. 5400–5408, Aug. 2020, doi: 10.1109/TGRS.2020.2965569.

[2] L. Toan et al., "The BIOMASS mission: Mapping global forest biomass to better understand the terrestrial carbon cycle," *Remote Sens. Environ.*, vol. 115, no. 11, pp. 2850–2860, Nov. 2011.

[3] Satellite Mission page of Biomass. [Online]. Available: https://directory.eoportal.org/web/eoportal/satellite-missions/b/biomass

[4] R. Shah et al., "Remote sensing of snow water equivalent using P-band coherent reflection," *IEEE Geosci. Remote Sens. Lett.*, vol. 14, no. 3, pp. 309–313, Mar. 2017.

[5] K. C. Jezek et al., "500–2000-MHz brightness temperature spectra of the Northwestern Greenland ice sheet," *IEEE Trans. Geosci. Remote Sens.*, vol. 56, no. 3, pp. 1485–1496, Mar. 2018, doi: 10.1109/TGRS.2017.2764381.

[6] M. Unwin, P. Jales, J. Tye, C. Gommenginger, G. Foti, and J. Rosello, "Spaceborne GNSS-reflectometry on TechDemoSat-1: Early mission operations and exploitation," *IEEE J. Sel. Topics Appl. Earth Observ. Remote Sens.*, vol. 9, no. 10, pp. 4525–4539, Oct. 2016, doi: 10.1109/JSTARS.2016.2603846.

[7] C. Ruf et al., "CYGNSS: Enabling the future of hurricane prediction [remote sensing satellites]," *IEEE Geosci. Remote Sens. Mag.*, vol. 1, no. 2, pp. 52–67, Jun. 2013.

[8] C. Jing, X. Niu, C. Duan, F. Lu, G. Di, and X. Yang, "Sea surface wind speed retrieval from the first Chinese GNSS-R mission: Technique and preliminary results," *Remote Sens.*, vol. 11, no. 24, Dec. 2019, Art. no. 3013.

[9] M. P. Clarizia and C. S. Ruf, "Wind speed retrieval algorithm for the cyclone global navigation satellite system (CYGNSS) mission," *IEEE Trans. Geosci. Remote Sens.*, vol. 54, no. 8, pp. 4419–4432, Aug. 2016.

[10] W. Li, E. Cardellach, F. Fabra, A. Rius, S. Ribo, and M. Martin-Neira, "First spaceborne phase altimetry over sea ice using TechDemoSat-1 GNSS-R signals," *Geophysical Res. Lett.*, vol. 44, no. 16, pp. 8369–8376, 2017.

[11] S. V. Nghiem et al., "Wetland monitoring with global navigation satellite system reflectometry: Wetland monitoring with GNSS-R," *Earth Space Sci.*, vol. 4, no. 1, pp. 16–39, 2017.

[12] H. Kim and V. Lakshmi, "Use of cyclone global navigation satellite system (CYGNSS) observations for estimation of soil moisture," *Geophysical Res. Lett.*, vol. 45, no. 16, pp. 8272–8282, 2018.

[13] C. C. Chew and E. E. Small, "Soil moisture sensing using spaceborne GNSS reflections: Comparison of CYGNSS reflectivity to SMAP soil moisture," *Geophysical Res. Lett.*, vol. 45, no. 9, pp. 4049–4057, 2018.

[14] M. P. Clarizia, N. Pierdicca, F. Costantini, and N. Floury, "Analysis of CYGNSS data for soil moisture retrieval," *IEEE J. Sel. Topics Appl. Earth Observ. Remote Sens.*, vol. 12, no. 7, pp. 2227–2235, Jul. 2019.

[15] A. Camps et al., "Sensitivity of GNSS-R spaceborne observations to soil moisture and vegetation," *IEEE J. Sel. Topics Appl. Earth Observ. Remote Sens.*, vol. 9, no. 10, pp. 4730–4742, Oct. 2016, doi: 10.1109/JSTARS.2016.2588467.

[16] X. Chu et al., "Multimodal deep learning for heterogeneous GNSS-R data fusion and ocean wind speed retrieval," *IEEE J. Sel. Topics Appl. Earth Observ. Remote Sens.*, vol. 13, pp. 5971–5981, 2020, doi: 10.1109/JSTARS.2020.3010879.

[17] S. H. Yueh, R. Shah, X. Xu, B. Stiles, and X. Bosch-Lluis, "A satellite synthetic aperture radar concept using P-band signals of opportunity," *IEEE J. Sel. Topics Appl. Earth Observ. Remote Sens.*, vol. 28, pp. 2796–2816, Feb. 2021, doi: 10.1109/JSTARS.2021.3059242.

[18] J. D. Oetting and T. Jen, "The mobile user objective system," *Johns Hopkins Appl. Phys. Lett. Tech. Dig.*, vol. 30, no. 2, pp. 103–112, 2011.

[19] J. Z. B. Ren, L. Tsang, and H. Xu, "Analytical Kirchhoff solutions (AKS) and numerical Kirchhoff approach (NKA) for first-principle calculations of coherent waves and incoherent waves at P band and L band in signals of opportunity (SoOp)," *Prog. Electromagn. Res.*, vol. 171, pp. 35–73, 2021.

[20] T. H. Painter and K. J. Bormann, "ASO L4 lidar point cloud digital terrain model 3m UTM grid, version 1 [data set]," 2020.

[21] L. Tsang, T.-H. Liao, R. Gao, H. Xu, W. Gu, and J. Zhu, "Theory of microwave remote sensing of vegetation effects, SoOp and rough soil surface backscattering," *Remote Sens.*, vol. 14, no. 15, 2022, Art. no. 3640, doi: 10.3390/rs14153640.

[22] M. M. Al-Khaldi, J. T. Johnson, A. J. O'Brien, A. Balenzano, and F. Mattia, "Time-series retrieval of soil moisture using CYGNSS," *IEEE Trans. Geosci. Remote Sens.*, vol. 57, no. 7, pp. 4322–4331, Jul. 2019.

[23] J. D. Campbell, A. Melebari, and M. Moghaddam, "Modeling the effects of topography on delay-Doppler maps," *IEEE J. Sel. Topics Appl. Earth Observ. Remote Sens.*, vol. 13, pp. 1740–1751, 2020, doi: 10.1109/JSTARS.2020.2981570.

[24] D. R. Thompson, T. M. Elfouhaily, and J. L. Garrison, "An improved geometrical optics model for bistatic GPS scattering from the ocean surface," *IEEE Trans. Geosci. Remote Sens.*, vol. 43, no. 12, pp. 2810–2821, Dec. 2005.

[25] L. Dente, L. Guerriero, D. Comite, and N. Pierdicca, "Space-borne GNSS-R signal over complex topography: Modeling and validation," *IEEE J. Sel. Topics Appl. Earth Observ. Remote Sens.*, vol. 13, pp. 1218–1233, 2020.

[26] W. Gu, H. Xu, and L. Tsang, "A numerical Kirchhoff simulator for GNSS-R land applications," *Prog. Electromagn. Res.*, vol. 164, pp. 119–133, 2019.

[27] J. D. Campbell et al., "Intercomparison of electromagnetic scattering models for delay-Doppler maps along a CYGNSS land track with topography," *IEEE Trans. Geosci. Remote Sens.*, vol. 60, 2022, Art. no. 2007413, doi: 10.1109/TGRS.2022.3210160.

[28] L. Tsang and J. A. Kong, *Scattering of Electromagnetic Waves Advanced Topics*, (Wiley Series in Remote Sensing). Hoboken, NJ, USA: Wiley, 2001.

[29] V. U. Zavorotny and A. G. Voronovich, "Scattering of GPS signals from the ocean with wind remote sensing application," *IEEE Trans. Geosci. Remote Sens.*, vol. 38, no. 2, pp. 951–964, Mar. 2000.

[30] L. Tsang, J. A. Kong, K. H. Ding, and C. O. Ao, *Scattering of Electromagnetic Waves: Numerical Simulations*. Hoboken, NJ, USA: Wiley, 2001.

Haokui Xu (Student Member, IEEE) received the B.S, degree in electrical engineering from the Beijing Institute of Technology, Beijing, China, in 2014, and the M.S. degree in electrical engineering from the University of Michigan, Ann Arbor, MI, USA, in 2016, where he is currently working toward the Ph.D. degree.

His research interests include wave scattering from terrestrial snow, thermal emission from polar ice sheet, and GNSS-R land applications.

Leung Tsang (Life Fellow, IEEE) was born in Hong Kong. He received the B.S., M.S., and Ph.D. degrees in electrical engineering from MIT, Cambridge, MA, USA, in 1971, 1973, and 1976, respectively.

He was with the University of Washington in 1983–2014 and was the Chair of the EE Department from 2006 to 2011. From 2001 to 2004, he was on leave at the EE Department of the City University of Hong Kong. Since 2015, he has been a Professor with the Department of EECS, University of Michigan, Ann Arbor, MI, USA. He is the lead author of four books: *Theory of Microwave Remote Sensing and Scattering of Electromagnetic Waves* (Volumes 12, and 3). His current research interests include remote sensing, random media and rough surfaces, computational electromagnetics, electromagnetic compatibility, and photonic crystals.

Dr. Tsang was the Editor-in-Chief of the IEEE TGARS from 1996 to 2000 and was the President of the IEEE Geoscience and Remote Sensing Society (GRSS) in 2006–2007. He is an honorary life member of GRSS. He has been the Chair of PIERS and the President of Electromagnetics Academy since 2008. He was the recipient of the Distinguished Achievement Award from GRSS in 2008, the Golden Florin Award in 2010, the William Pecora Award co-sponsored by USGS and NASA in 2012, the IEEE Electromagnetics Award in 2013, and the van de Hulst Light Scattering Award in 2018. He is a Fellow of the Optical Society of America and a member of the U.S. National Academy of Engineering.

Xiaolan Xu (Senior Member, IEEE) received the B.Eng. degree in electrical engineering from the Zhejiang University in China, Hangzhou, China, in 2006, and the M.S. and Ph.D. degrees in electrical engineering from the University of Washington, Seattle, WA, USA, in 2008 and 2011, respectively.

In 2012, she joined the Jet Propulsion Laboratory (JPL), California Institute of Technology, Pasadena, CA, USA, as a Postdoctoral Research Associate and has been a Scientist since 2014. Her research interests include applied electromagnetics, electromagnetic wave propagation, and scattering properties from snow-covered terrain, vegetated land surface, and bare soil. She specialized in the development of forward modeling and retrieval algorithm with applications to Earth remote sensing from space.

Dr. Xu was the recipient of the URSI Santimay Basu Award in 2020.

Simon H. Yueh (Fellow, IEEE) received the Ph.D. degree in electrical engineering from the Massachusetts Institute of Technology, Cambridge, MA, USA, in 1991.

He was a Postdoctoral Research Associate with the Massachusetts Institute of Technology, from February to August 1991. In 1991, he joined the Radar Science and Engineering Section, Jet Propulsion Laboratory (JPL). He was the Supervisor of radar system engineering and algorithm development group from 2002–2007, the Deputy Manager of Climate, Oceans and Solid Earth section from 2007 to 2009, and the Section Manager from 2009 to 2013. He served as the Project Scientist of the National Aeronautics and Space Administration (NASA) Aquarius mission from 2012 to 2013, the Deputy Project Scientist of NASA Soil Moisture Active Passive Mission from January 2013 to September 2013, and the SMAP Project Scientist since October 2013. He has been the Principal/Co-Investigator of numerous NASA and DOD research projects on remote sensing of ocean salinity, ocean wind, terrestrial snow and soil moisture. He has authored 4 book chapters and published more than 300 publications and presentations.

Dr. Yueh was the refcipient of the 2021 IEEE J-STARS Prize Paper Award, the 2014 IEEE GRSS Transaction Prize Paper Award, the 2010 IEEE GRSS Transaction Prize Paper Award, the 2002 IEEE GRSS Transaction Prize Paper Award, the 2000 Best Paper Award in IEEE International Geoscience and Remote Symposium 2000, the 1995 IEEE GRSS Transaction Prize Paper Award for a paper on polarimetric radiometry, the JPL Lew Allen Award in 1998, the Ed Stone Award in 2003, the NASA Exceptional Technology Achievement Award in 2014, and the NASA Outstanding Public Leadership Medal in 2017. He was an Associate Editor of Radio Science from 2002 to 2006 and the Editor in Chief of IEEE TRANSACTIONS ON GEOSCIENCE AND REMOTE SENSING from 2018–2022. He is a member of URSI Commission-F.

Steven A. Margulis received the B.S. degree in civil and environmental engineering from the University of Southern California, Los Angeles, CA, USA, in 1996, and the M.S. and Ph.D. degrees in civil and environmental engineering from the Massachusetts Institute of Technology, Cambridge, MA, USA, in 1998 and 2002, respectively.

He is currently a Professor and Vice Chair with the Department of Civil and Environmental Engineering, University of California, Los Angeles, CA, USA.

Rashmi Shah (Senior Member, IEEE) received the B.S. degree in electrical engineering from the Rochester Institute of Technology, Rochester, NY, USA, in 2007, and the M.S. and Ph.D. degrees in aeronautical and astronautical engineering from Purdue University, West Lafayette, IN, USA, in 2010 and 2014, respectively.

Since 2014, she has been a Research Technologist with Tracking Systems and Applications Section, Jet Propulsion Laboratory (JPL), California Institute of Technology (Caltech), Pasadena, CA, USA. She is also a part of the core team member for JPL Foundry's A-team where she works with teams on early concept development. Her background and research interests include microwave remote sensing, electromagnetic scattering, remote sensing using signals of opportunity reflectometry, and microwave remote sensing instrument development.

Dr. Shah was a recipient of the NASA Early Career Public Achievement Medal and the Institute of Electrical and Electronics Engineers (IEEE) Geoscience and Remote Sensing Society's (GRSS) Early Career Award. She also serves as the Co-Chair of the GNSS and Signals of Opportunity Working Group for the IEEE GRSS Society's Instrumentation and Future Technologies Technical Committee. She also serves as the Chapter Chair of IEEE Metropolitan Los Angeles GRSS Chapter.